




Ultra-high sensitive and ultra-low NO₂ detection at low-temperature based on ultrathin In₂O₃ nanosheets

PeiJiang Cao¹, RongGuan Chen¹, YongZhi Cai¹, Dnyandeo Pawar^{1,2,*} , Ch. N. Rao¹, Shun Han¹, WangYin Xu¹, Ming Fang¹, XinKe Liu¹, YuXiang Zeng¹, WenJun Liu¹, DeLiang Zhu¹, and YouMing Lu^{1,*}

¹ College of Materials Science and Engineering, Shenzhen University; Shenzhen Key Laboratory of Special Functional Materials, Shenzhen Engineering Laboratory for Advanced Technology of Ceramics and Guangdong Research Center for Interfacial Engineering of Functional Materials, Shenzhen 518055, People's Republic of China

² Key Laboratory of Optoelectronic Devices and Systems of Ministry of Education and Guangdong Province, College of Optoelectronic Engineering, Shenzhen University, Shenzhen 518055, People's Republic of China

Received: 20 April 2021

Accepted: 20 June 2021

Published online:

3 July 2021

© The Author(s), under exclusive licence to Springer Science+Business Media, LLC, part of Springer Nature 2021

ABSTRACT

In this study, the high oxygen vacancy-rich ultrathin indium oxide (In₂O₃) nanosheets are synthesized by low-cost and environmental-friendly solvothermal method. The gas sensing properties of In₂O₃ nanosheets to low concentration of nitrogen dioxide (NO₂) (concentration in 5 ppb to 5 ppm) at 50 °C are investigated. All In₂O₃ samples are successfully characterized using various techniques to obtain the information related to phase, morphological, oxygen vacancies, and surface area, etc. It is observed that among all the samples, the In₂O₃-350 exhibited benchmarked response of around 3223 at 2 ppm NO₂ gas, with theoretical detection limit down to ppb level. The sensor has shown superior sensing characteristics, such as wide sensing bandwidth, excellent selectivity, high long-term stability, and good repeatability. It is considered that the high oxygen deficiency present on In₂O₃ nanosheets acts as favorable reaction sites for such remarkable sensing performance, and therefore, these improved gas-sensing properties make the In₂O₃ nanosheets suitable to detect NO₂ at low-temperature.

1 Introduction

Rapid industrialization and urbanization have resulted in pollution across the globe and thus, causing serious impact on human life and environment. It is believed that the automobile industries are

the main sources for releasing the number of toxic gases in the earth atmosphere. Among the various gases, nitrogen dioxide (NO₂) originated from the smog and acid rain is considered to be highly toxic and extremely dangerous to plants, humans and aquatic animals, when NO₂ concentration goes above the level of 50 ppb [1]. As per the Occupational Safety

Address correspondence to E-mail: pawar.dnyandeo@gmail.com; ymlu@szu.edu.cn

and Health Administration (OSHA), USA, the threshold limit and tolerable short-term exposure is around 3 and 1 ppm for < 15 min of NO₂ gas [2]. By using a reliable sensory platform, one could detect such tiny NO₂ concentration with high accuracy and great stability. Therefore, the sensor with lower detection limit, high sensitivity, and excellent selectivity is highly required for effective monitoring of NO₂ gas.

It is determined that numerous techniques have been utilized for NO₂ gas sensing. The resistive-based sensors fabricated by using semiconductor metal oxides have attracted tremendous attention for gas sensing due to their exceptional advantages, such as low cost, ease in fabrication, simple and effective geometry, low power requirement, immune to temperature and humidity environment, and easy deployment [3–5]. A number of metal oxides such as ZnO [6], CuO [7], SnO₂ [8], TiO₂ [9], WO₃ [10], Fe₂O₃ [11], NiO [12], and indium oxide (In₂O₃) [13] have been widely studied in gas sensing, especially for NO₂ sensing. However, most of these sensors possess certain limitations, such as need to operate at high working temperature (> 100 °C), exhibit less response value, and poor selectivity. Therefore, constructing a gas sensing device by utilizing metal oxides is a great challenge. Among the metal oxides, In₂O₃ offers very reliable gas sensing characteristics. It is an ideal gas sensing material, especially in the detection of NO₂ gas due to its higher affinity (2.28 eV) of NO₂ than pre-adsorbed oxygen (0.43 eV), high electrical conductivity, chemical stability and intrinsic defects [14]. In₂O₃ is an n-type direct band gap semiconductor originated from the oxygen vacancies (abundance dynamic sites) present on its surface, which act as donor levels to provide free electrons to the conduction band of In₂O₃ and hence, increases the adsorption of NO₂ [15–17]. So, various In₂O₃-based sensors have been explored for NO₂ gas sensing [18–25]. Among these sensors, few are working at high temperature and therefore, not feasible to use for gas sensing due to risk associated at high temperature [18–21]. Some operate at room temperature but its sensing response is low and therefore, need further improvement [22, 23]. Few sensors fabricated by doping the metals in In₂O₃ to further enhance the sensing performance, but still they are not highly efficient [24, 25]. Few sensors

show poor selectivity and therefore, restrict the development of an ideal NO₂ gas sensor. Therefore, our aim is to synthesize highly sensitive and stable In₂O₃ nanostructure for selective detection of NO₂ near room temperature.

In this work, we reported the synthesis of In₂O₃ nanosheets by using a solvothermal method. The In₂O₃ nanosheets with enriched in oxygen vacancies were utilized to detect the wide range of NO₂ gas with high response and selectivity near room temperature at 50 °C. The sensor has shown very high linear response and able to detect ppb level of NO₂ gas. The detailed experimental results and sensing mechanism of In₂O₃ with NO₂ gas are discussed.

2 Experimental

2.1 Synthesis of In₂O₃ nanosheets

The synthesis procedure of In₂O₃ nanosheets is shown in Fig. 1. Briefly, 0.4715 g of InCl₃·4H₂O dissolved in 72 mL of ethanol, in which the 0.6667 g sodium laurylsulfonate and 0.5334 g urea were added in the solution. Then, this mixture was stirred for 4 h followed by ultrasound treatment for 1.5 h. Later, the homogeneous solution transferred to and sealed in a Teflon-lined steel autoclave, which was kept in oven at 120 °C for 11 h. After completion of the reaction, the autoclave cooled down to room temperature naturally and the precipitate was collected by centrifugation process, and then further dried at 60 °C for 12 h [26]. Finally, the sample was calcinated at 350 °C, 400 °C, 450 °C, 500 °C, respectively, under controlled heating rate of 2 °C min⁻¹ for 2 h. The corresponding samples were named as In₂O₃-350, In₂O₃-400, In₂O₃-450, and In₂O₃-500, respectively. These samples were further analyzed by various characterization techniques.

2.2 Device fabrication and testing

The detail device fabrication is described in Fig. S11. Firstly, the paste was obtained by mixing certain amount of In₂O₃ powder in ethanol. Secondly, by using a thin brush, the paste was coated on a ceramic tube having length of 4 mm and diameter ratio of 0.8/1.2 mm with fixed Au-Pt electrodes. Then, a Ni-Cr coil was inserted into the ceramic tube, which

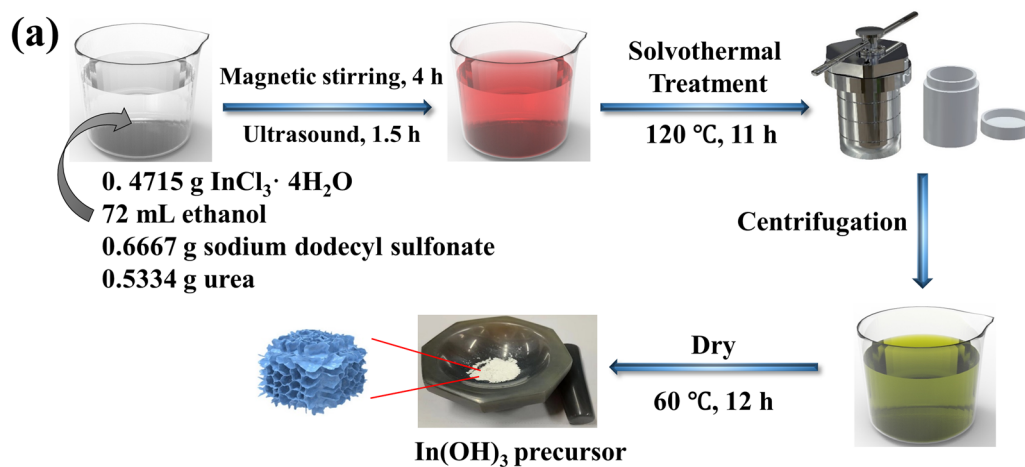
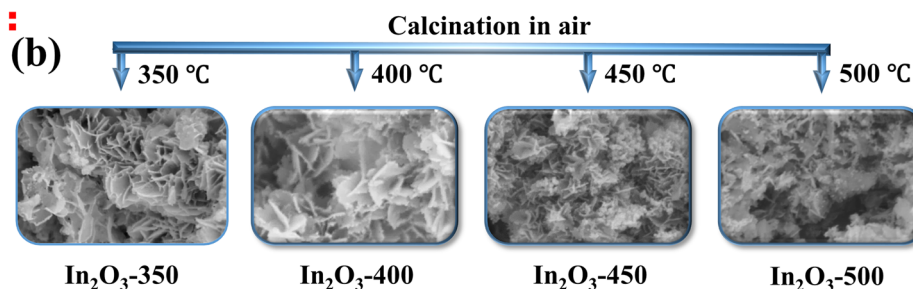
Step 1 :**Step 2 :**

Fig. 1 Schematic illustration for synthesis of In_2O_3 nanosheets

worked as a heater to control the working temperature of the sensing device. Finally, the fabricated product was aged at 110 °C for 48 h.

The resistive measurement system (CGS-8) having resistance bandwidth (1 Ω to 4 G Ω) was used to measure the sensing response. This system consisting of a gas chamber (volume: 20 L), where the fabricated sensor was positioned into the gas sensing holder. The sensor performance was studied under controlled amount of NO_2 gas at working temperature of 50 °C and under constant humidity at 30% RH. The NO_2 gas was purged inside the gas chamber by using a calibrated air-tight syringe (0–10 μL) (Shanghai Gaoe Industry and Trade Co., Ltd. China). The sensing performance was also measured under varied humidity environment. The gas response of the sensor is defined as follows: $R = R_g/R_a$ (when $R_g > R_a$) [27]. The response time is calculated by the time taken to reach 90% of its total change in resistance and recovery time is measured from time taken to recover to its 10% total change in resistance value.

3 Results and discussion

3.1 XRD, SEM and BET analysis

The crystalline phase confirmation of In_2O_3 is done by using X-ray diffractometer (XRD, Bruker, Germany, D8 Advance SS 18 KW, X-ray source: Cu K α , $\lambda = 0.15406$ nm) as shown in Fig. 2a. The diffraction peaks of In_2O_3 -300, In_2O_3 -350, In_2O_3 -400, In_2O_3 -450, and In_2O_3 -500 are well coincides with the JCPDS card no: 71–2194 of cubic In_2O_3 crystal structure [28, 29]. The diffraction pattern of pure In_2O_3 nanosheets exhibits major peaks at 21.49, 30.58, 35.46, 37.69, 45.68, 51.02, and 60.66, which corresponds to (211), (222), (400), (411), (431), (440), and (622) planes, respectively. Additionally, the sample description and its corresponding parameters calculated from XRD patterns are shown in Table SI1. The samples show the crystallite size of around 10 nm, 11 nm, 12 nm, 13 nm and 14 nm for In_2O_3 -300, In_2O_3 -350, In_2O_3 -400, In_2O_3 -450, and In_2O_3 -500, respectively. The XRD pattern of In_2O_3 -300 confirmed that the sample was not in phase of pure In_2O_3 . The strain generated in the materials is also measured from

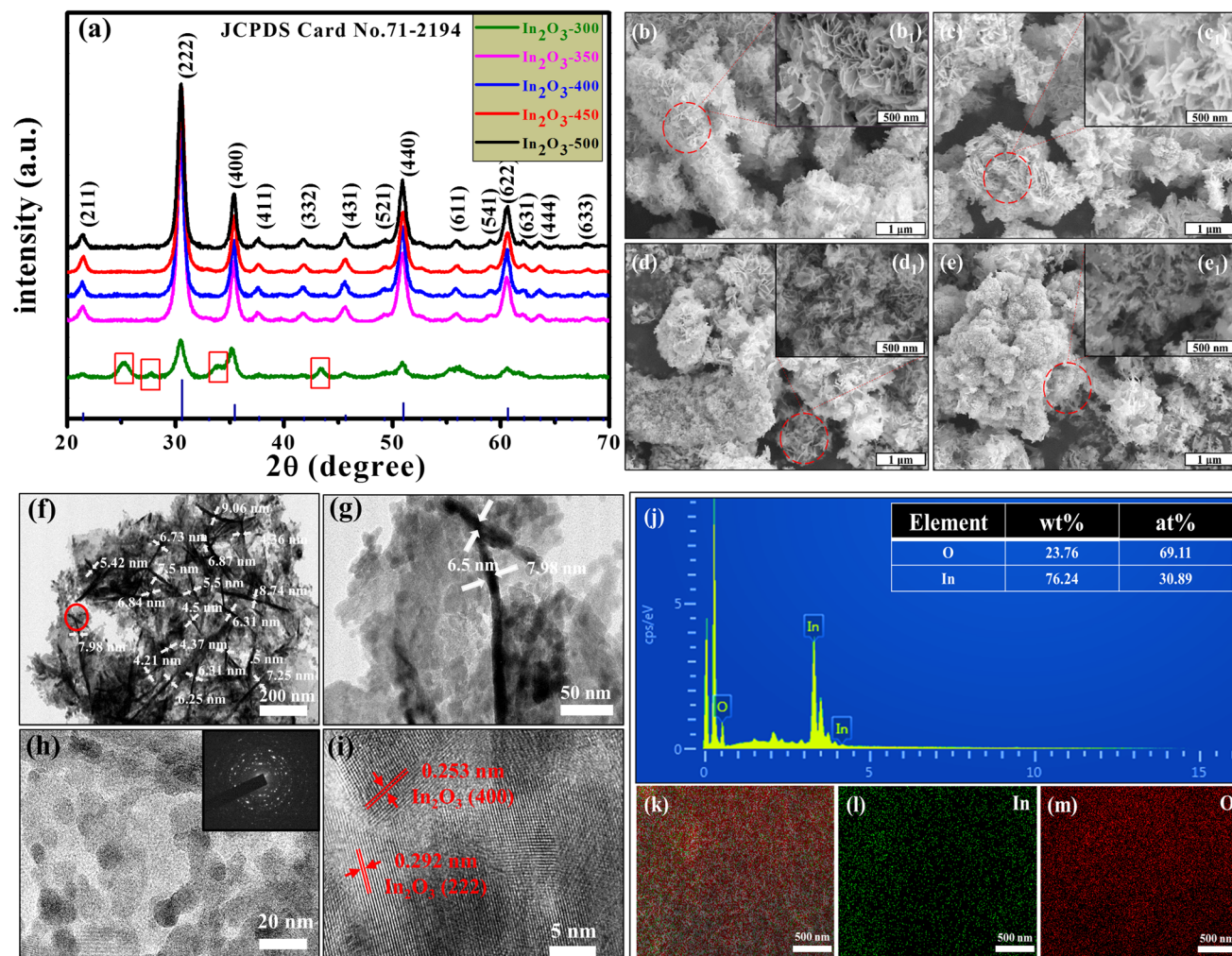


Fig. 2 a XRD patterns In_2O_3 -300, In_2O_3 -350, In_2O_3 -400, In_2O_3 -450, and In_2O_3 -500 samples of sensing materials; Typical SEM images of b In_2O_3 -350, c In_2O_3 -400, d In_2O_3 -450, and e In_2O_3 -500 (Inset shows enlarged images for (b1) In_2O_3 -350, (c1) In_2O_3 -400, (d1) In_2O_3 -450, and (e1) In_2O_3 -500); f and g Typical TEM images of In_2O_3 -350 sample; h HRTEM images of In_2O_3 -350

sample (inset of (h) shows SAED pattern of In_2O_3 -350); i Fringe pattern of In_2O_3 -350 sample; j EDS elemental mapping pattern for In_2O_3 -350 (inset shows the table containing wt% and at% of In and O in In_2O_3 -350); k Elemental mapping of C, In and O in In_2O_3 -350 sample; l, m shows the element mapping images of In and O in In_2O_3 -350

XRD spectrums and it is calculated around 0.0259, 0.023, 0.204, 0.0194, and 0.0188 for In_2O_3 -300, In_2O_3 -350, In_2O_3 -400, In_2O_3 -450, and In_2O_3 -500, respectively. The strain is observed to be decreased for In_2O_3 -300, In_2O_3 -350, In_2O_3 -400, In_2O_3 -450, and In_2O_3 -500 samples, as it is strongly related to the trapped impurities at nonequilibrium sites. The dislocation density that also indicates the amounts of defect is calculated as shown in Table SI1. The values are observed around 0.00968/nm, 0.00765/nm, 0.00604/nm, 0.00549/nm, and 0.00513/nm for In_2O_3 -300, In_2O_3 -350, In_2O_3 -400, In_2O_3 -450, and In_2O_3 -500 samples, respectively. The UV–vis spectrum (Perkin

Elmer Lambda 950) of In_2O_3 -350 displays an absorbance peak at 307 nm as shown in Fig. SI2a. The bandgap of In_2O_3 calculated from Tauc plot is observed around 3.14 eV as depicted in Fig. SI2b.

The morphology of sensing materials is studied by using scanning electron microscope (SEM, Hitachi SU-70) and transmission electron microscope (TEM, JEM-1230 microscopy). Figure SI3 shows the SEM image of In_2O_3 precursor before calcination. It shows that the In_2O_3 sample looks like a nanosheet structure. The superior morphology of In_2O_3 is obtained by annealing the In_2O_3 precursor at different temperatures 350 °C, 400 °C, 450 °C, and 500 °C,

respectively. The morphology of In_2O_3 -350, In_2O_3 -400, In_2O_3 -450, and In_2O_3 -500 is shown in Fig. 2b, c, d, e. Very fine morphology is observed for In_2O_3 -350 as compared with other samples. It also displays the variation in porosity with respect to annealing temperature. As temperature rises, the nanosheets break and its porosity appears to be decreased. The TEM images depicted in Fig. 2f, g, h, i reveal the morphology, clear lattice fringe pattern and lattice fringe spacing of In_2O_3 -350 sample. The In_2O_3 -350 shows the thickness of less than 10 nm. The SAED pattern of In_2O_3 -350 shows the polycrystalline nature as shown in an inset of Fig. 2h. The lattice fringe pattern and fringe spacing of In_2O_3 -350 are shown in Fig. 2i. It shows that the fringe spacing is observed around 0.253 nm and 0.292 nm, which corresponds to (400) and (222) planes of cubic In_2O_3 structure. The elemental composition is investigated by energy dispersive X-ray spectroscopy (EDS) (Hitachi SU-70). The elemental distribution for In_2O_3 -350 is presented in Fig. 2j. The full EDS pattern of In_2O_3 -350 and at% of each element corresponding to In and O is depicted in Fig. 2k, l, and m. The distribution of In (30.89%) and O (69.11%) is detected for In_2O_3 -350 nearby to at% ratio of In/O elements in In_2O_3 molecule, which verified that the prepared sample is In_2O_3 only.

The N_2 adsorption/desorption and pore size dispersal study of In_2O_3 -350 test sample is done by using Brunauer–Emmett–Teller (BET) instrument (Micrometrics ASAP 2020). The characteristics type-IV curve with a hysteresis loop is observed in N_2 adsorption/desorption curve of In_2O_3 -350 nanosheets as shown in Fig. SI4a. This type of curve specifies the existence of mesoporous structure [30, 31]. The BET surface area of $52.01 \text{ m}^2/\text{g}$ is detected for In_2O_3 -350 sample. The BJH pore size distribution of In_2O_3 -350 nanosheets is shown in Fig. SI4b. It displays that the nanosheets possess wide pore-size distribution varying from 2 nm to 80 nm.

3.2 XPS results

X-ray photoelectron spectroscopy (XPS) (Microlab 350 Auger Spectrometer, Thermo Fisher, USA) measurement is used to study the elemental and bonding of In_2O_3 test samples. The full survey spectrum of all In_2O_3 samples is shown in Fig. 3a. It is observed that the Indium (In), oxygen (O), and carbon (C) peaks are present without any other elemental peaks, which confirmed the high purity of the sample. Figure 3b

shows the spectrum of In for all In_2O_3 samples. As the annealing temperature increases, the corresponding peak position is shifted toward higher binding energy side. It reveals that the In $3d_{5/2}$ and In $3d_{3/2}$ peaks are positioned at 444.2 eV and 451.8 eV, which are ascribed to In^{3+} state in In_2O_3 [32, 33]. In this work, the oxygen vacancies present on the surface of In_2O_3 play major role, which considered to be one of the deciding factor in gas sensing performance. Therefore, the O 1s spectrum for In_2O_3 samples is shown in Fig. 3c, d, e, f. For all samples, the O 1s peak is best fitted in three major peaks, namely crystal lattice oxygen (O_L) of In-O, oxygen vacancy (O_V) and chemisorbed oxygen species (O_C) of (H_2O , O_2) present on the surface of In_2O_3 . For all In_2O_3 samples, the peak position of O_L is observed at 529.4–529.8 eV, the O_V peak is observed in between 530.9 eV and 531.3 eV, and O_C peak is located in between 531.9 eV and 532.3 eV [34, 35]. The XPS study also investigates that the In_2O_3 -350 test sample shows high relative percentage of oxygen vacancy (36.3%) present on its surface as compared with (29.86%) for In_2O_3 -400, (28.09%) for In_2O_3 -450, and (24.68%) for In_2O_3 -500, respectively. The relative percentage of O_L , O_V and O_C present in all In_2O_3 samples are provided in Table SI2. Thus, higher the percentage of O_V and O_C , larger the interaction with NO_2 gas and thus, greater the gas sensing performance.

3.3 Gas sensing characteristics of In_2O_3 nanosheets

Generally, the working temperature is very crucial in gas sensing domain. To optimize the working temperature, the fabricated In_2O_3 -350, In_2O_3 -400, In_2O_3 -450, and In_2O_3 -500 sensors have been tested under exposure of 2 ppm of NO_2 gas and humidity at 30% RH in the temperature range of 30 °C to 100 °C as shown in Fig. 4a. It is examined that the response of sensors rises and reach maximum at specific temperature, and then starts decreasing with increase in temperature. The nature of curve depends upon the thermodynamics of gas adsorption and desorption mechanism. It observed that the In_2O_3 -350 sample has shown highest sensing response of ($S = 3223$ to 2 ppm NO_2 gas), as compared with other test samples of In_2O_3 -400 ($S = 1838$), In_2O_3 -450 ($S = 1064$), and In_2O_3 -500 ($S = 558$), respectively. It is remarkable that the In_2O_3 -350 sensor exhibits highest sensing

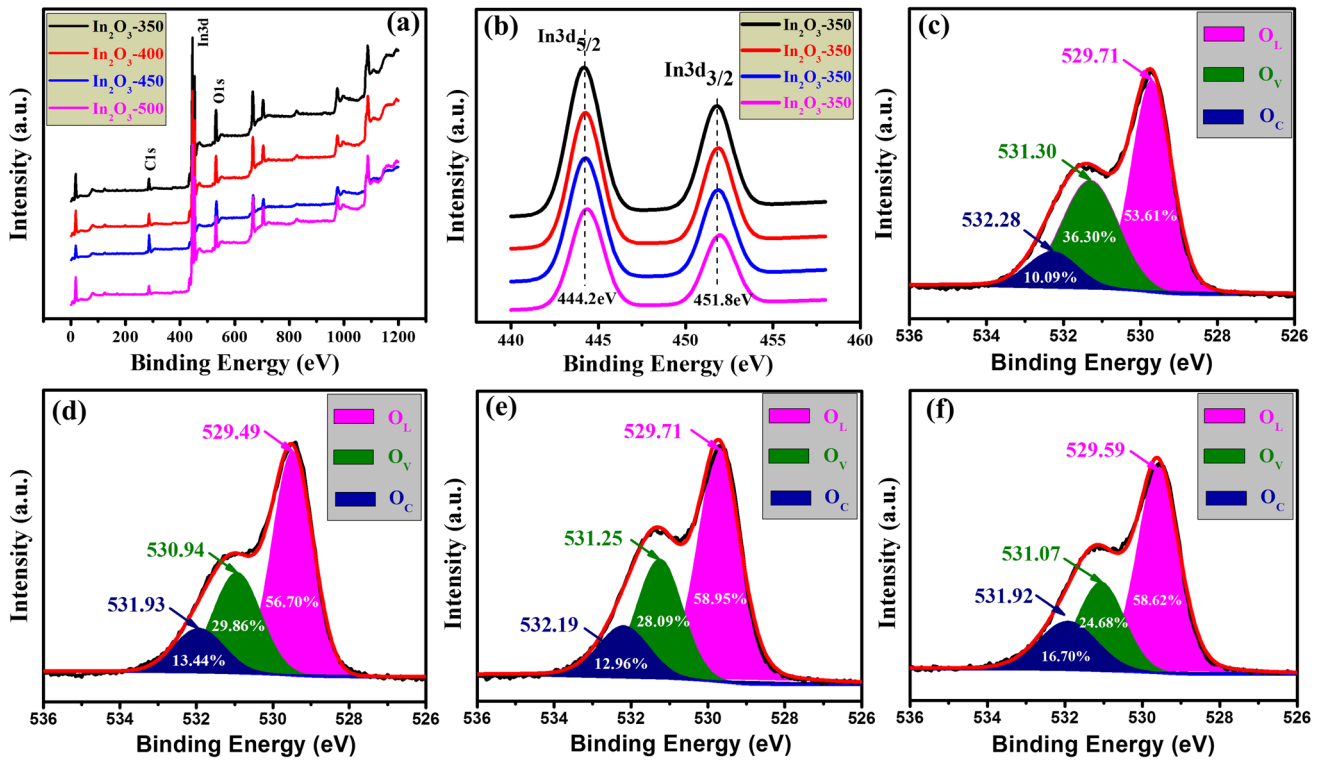


Fig. 3 The XPS survey including **a** Full survey spectrum of In_2O_3 -350, In_2O_3 -400, In_2O_3 -450, and In_2O_3 -500; **b** High resolution spectra of In for In_2O_3 -350, In_2O_3 -400, In_2O_3 -450,

and In_2O_3 -500; and high-resolution spectra of oxygen for **c** In_2O_3 -350; **d** In_2O_3 -400; **e** In_2O_3 -450, and **f** In_2O_3 -500, respectively

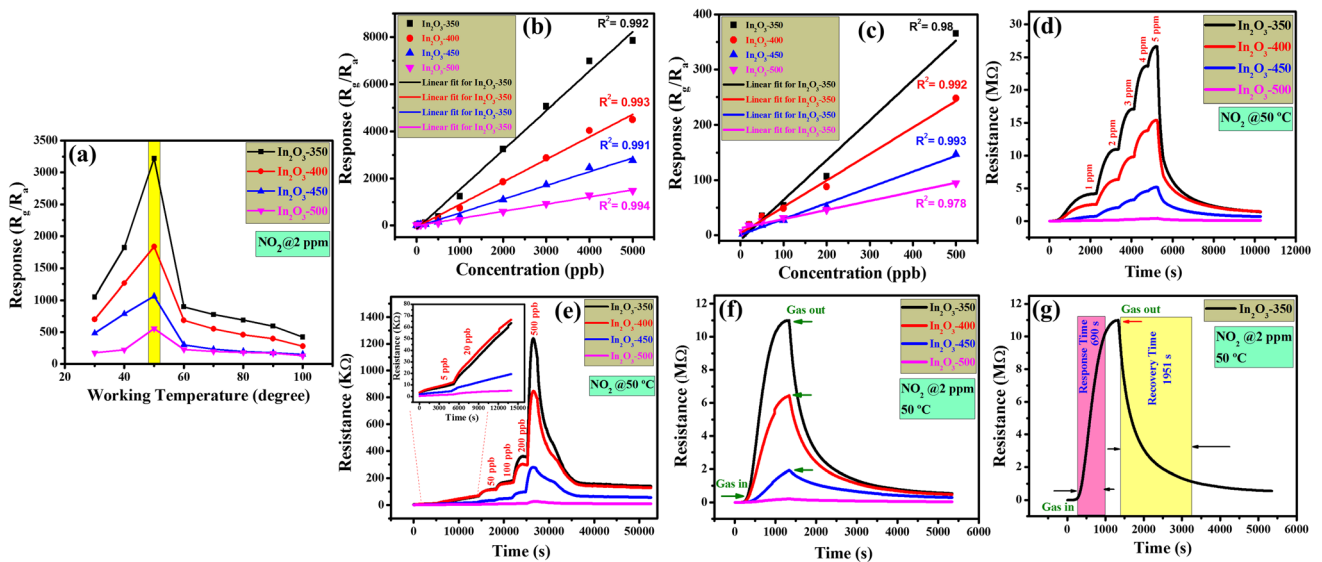


Fig. 4 **a** Response of In_2O_3 -350, In_2O_3 -400, In_2O_3 -450, and In_2O_3 -500 sensors to 2 ppm NO_2 gas at various working temperature; **b** Sensor response of In_2O_3 -350, In_2O_3 -400, In_2O_3 -450, and In_2O_3 -500 under exposure of NO_2 gas in 5 ppb to 5000 ppb; **c** Sensing performance of In_2O_3 -350, In_2O_3 -400, In_2O_3 -450, and In_2O_3 -500 in ppb level NO_2 gas in the range of 5 ppb to 500 ppb; **d** Time resistance curves of In_2O_3 -350, In_2O_3 -400, In_2O_3 -450, and In_2O_3 -500 in NO_2 gas of 1 ppm to 5 ppm at 50 °C;

e Temporal resistance response curves of In_2O_3 -350, In_2O_3 -400, In_2O_3 -450, and In_2O_3 -500 sensor under the exposure of NO_2 gas concentration ranging from 5 to 500 ppb (The inset image in **e** shows the time response characteristics to 5 ppb and 20 ppb NO_2 gas concentration); **f** Time response/recovery curves of In_2O_3 -350, In_2O_3 -400, In_2O_3 -450, and In_2O_3 -500 to 2 ppm NO_2 gas and **g** Time response/recovery curves of In_2O_3 -350 sensor under 2 ppm NO_2 gas at working temperature of 50 °C

response toward 2 ppm at very low operating temperature, and therefore, the 50 °C was selected as a best optimized temperature for all test samples.

The temporal resistance curves of In₂O₃-350, In₂O₃-400, In₂O₃-450, and In₂O₃-500 test samples to NO₂ in the range of 5 ppb to 5 ppm at optimal temperature of 50 °C and humidity at 30% RH are shown in Fig. S15. It demonstrates that as the NO₂ concentration increases, the corresponding resistance of In₂O₃ nanosheets also rises. The In₂O₃-350 test sample shows very high change in the resistance value. The response (R_g/R_a) (temporal response curve is shown in Fig. S16) for In₂O₃-350, In₂O₃-400, In₂O₃-450, and In₂O₃-500 is calculated by using the resistance values as shown in Fig. S15. It indicates that more change in the resistance of sensing material, more is the response value. Among them, In₂O₃-350 has shown enhanced in response as compared with In₂O₃-400, In₂O₃-450, and In₂O₃-500 test samples. The response and recovery time of all test samples is investigated from their respective time response curves. The detailed analysis of response/recovery time is discussed below.

Figure 4b demonstrates the response behavior of fabricated In₂O₃-350, In₂O₃-400, In₂O₃-450, and In₂O₃-500 test samples under the exposure of 5 ppb to 5000 ppb of NO₂. All sensors exhibit excellent linear relationship with wide range of NO₂ gas, indicating its potential use for gas sensing. The In₂O₃-350 test sample shows highest sensing response as compared with In₂O₃-400, In₂O₃-450, and In₂O₃-500 test samples. The response value of each sensor is measured around 7845.3 ($R^2 = 0.992$) for In₂O₃-350, 4507.11 ($R^2 = 0.993$) for In₂O₃-400, 2762.34 ($R^2 = 0.991$) for In₂O₃-450, and 1473.06 ($R^2 = 0.994$) for In₂O₃-500, respectively. It indicates that the In₂O₃-350 exhibits very high linearity with obtained response of around 1.674/ppb as that of 0.958/ppb for In₂O₃-400, 0.584/ppb for In₂O₃-450, and 0.305/ppb for In₂O₃-500, respectively. The error in the response value was $\sim \pm 5\%$. The value of detection limit for all sensors is calculated by using equations reported elsewhere [36, 37]. The detail discussion regarding calculation of theoretical detection limit is provided in the supplementary information. The theoretical detection limit for In₂O₃-350 is calculated around 1.5 parts-per-trillion (ppt), whereas for other sensors it is around 2.1 ppt, 10.16 ppt, and 19.85 ppt for In₂O₃-400, In₂O₃-450, and In₂O₃-500 samples, respectively. To best of our knowledge, the reported response value and

theoretical detection limit are the highest values stated so far based on In₂O₃ utilized resistive-based approach. Considering the application point of view, it is highly desirable to detect low concentration of NO₂ gas, and therefore, the sensing behavior of all the test samples in lower concentration regime of NO₂ gas is revealed in Fig. 4c. It is noted that these sensors shown very high sensing response in lower range (5–500 ppb) of NO₂, as depicted in Fig. 4c. Among all the sensors, In₂O₃-350 exhibits very high linearity with obtained response of around 0.721/ppb ($R^2 = 0.98$), as that of response values around 0.479/ppb ($R^2 = 0.992$) for In₂O₃-400, 0.286/ppb ($R^2 = 0.993$) for In₂O₃-450, and 0.165/ppb ($R^2 = 0.978$) for In₂O₃-500, respectively. Therefore, the In₂O₃-based sensors are very effective and potential candidate to detect very low concentration of NO₂ gas. In detail, the response values of In₂O₃-350, In₂O₃-400, In₂O₃-450, and In₂O₃-500 sensors to 5 ppb–5 ppm NO₂ are displayed in Table S13. The comparison of NO₂ sensing performance between our sensor with the other reported sensors is tabulated in Table 1. The comparison of NO₂ gas sensing characteristics between our work and earlier reports based on various metal-oxides nanostructures is summarized in Table S14. Additionally, the sensing performances of some developed sensors based on only In₂O₃ toward NO₂ are depicted in Table S15. As can be seen from the tables, our fabricated sensor exhibits better sensing performance than those earlier reported sensors.

The response/recovery characteristics of In₂O₃ nanosheets to NO₂ concentration of 5 ppb to 5 ppm are shown in Fig. 4d, e. It demonstrates that with respect to increase in concentration of NO₂, the corresponding resistance of In₂O₃ nanosheets also changes. Therefore, with respect to increase in NO₂ concentration, the corresponding response is also increased. The time resistance response curves for all In₂O₃ test samples of In₂O₃-350, In₂O₃-400, In₂O₃-450, and In₂O₃-500 in high range of NO₂ (1 ppm to 5 ppm) are displayed in Fig. 4d. The temporal resistance response in lower concentration (5 ppb to 500 ppb) for all test samples is shown in Fig. 4e. The response of all test sensors in 5 ppb to 20 ppb is shown in an inset of Fig. 4e. It is observed that as the concentration of NO₂ gas increased, the corresponding sensor resistance is also enlarged. When NO₂ is purged inside the gas chamber, the response of sensors steadily increases and reaches saturation due to the

Table 1 Comparison of NO₂ sensing performances between our fabricated sensor and previously reported sensors based on various metal-oxides nanostructures

Sample	Morphology	Synthesis method	Temp. (°C)	LOD	Res-t (s)/Rec-t (s)	Response (conc.)
WO ₃ [38]	Porous nanosheet arrays	Chemical bath deposition	100	1 ppm	54/63	460 (10 ppm)
SnO ₂ -Sn ₃ O ₄ [39]	Heterostructure	Solvothermal	150	20 ppb	117/55	240 (5 ppm)
Au-TiO ₂ [40]	Nanorods	Wet-chemical	250	500 ppb	40/43	136.5 (5 ppm)
WO ₃ [41]	Dendrites	Solvothermal	170	200 ppb	7/12	32.9 (5 ppm)
ZnO-TiO ₂ [42]	Nanorods	Hybrid method	180	/	14/6	350 (100 ppm)
In ₂ O ₃ [43]	Hierarchical nanorod-flowers	Hydrothermal	145	0.2 ppm	60/30 (1 ppm)	132 (1 ppm)
In ₂ O ₃ (This work)	Nanosheets	Solvothermal	50	5 ppb	690/1951 (2 ppm)	3227 (2 ppm)

ratio of oxygen ions and NO₂ molecules. When sensor is exposed to air, the sensor response is decreased and achieves its initial state. The response time curves for In₂O₃-350, In₂O₃-400, In₂O₃-450, and In₂O₃-500 are shown in Fig. S17. To determine response/recovery time of these sensors, their combined graphs have been plotted as shown Fig. 4f. The response/recovery time of each sensor is calculated from their respective resistance curves. The resistance response/recovery time graphs for In₂O₃-350, In₂O₃-400, In₂O₃-450, and In₂O₃-500 are shown in Fig. S18. It displays that the In₂O₃-350 shows less response/recovery time around (690 s/1951s), as compared with other In₂O₃ samples of In₂O₃-400 (844 s/2511 s), In₂O₃-450 (935 s/3114 s), and In₂O₃-500 (972 s/3354 s) to 2 ppm NO₂ gas at 50 °C. Figure 4g shows the time response characteristics of In₂O₃-350, indicating that the In₂O₃-350 sample displays much enhanced time response characteristics with remarkable sensing performance as that of other test samples.

The good repeatability is also one of the significant criteria in gas sensing. An excellent repeatability of In₂O₃-350 sample over five repeatable cycles under exposure of 2 ppm at 50 °C and at humidity of 25% RH is displayed in Fig. 5a. For all five repeatable cycles, the average error obtained in the maximum response values are 3234.47 ± 7.51, 3227.5 ± 14.48, 3234.47 ± 7.51, 3231.74 ± 10.24, and 3281.72 ± 39.74, respectively. The repeatability test for other samples of In₂O₃-400, In₂O₃-450, and In₂O₃-500 is shown in Fig. S19, confirming that these sensors are also highly repeatable.

The good selectivity is a very significant parameter for any type of gas sensor. While studying the selectivity, each test sample is exposed toward 2 ppm NO₂ and 100 ppm of other interfering gases including acetone, methanol, ethanol, NH₃, SO₂, and CO₂, respectively, as display in Fig. 5b. In detailed, the response of around 3223 for In₂O₃-350, 1838 for In₂O₃-400, 1064 for In₂O₃-450 and 558 for In₂O₃-500 to 2 ppm of NO₂ gas is observed. Whereas, for other intrusive gases (like acetone, methanol, ethanol, NH₃, SO₂, and CO₂), the response value of around ≤ 1.2 is measured. Therefore, it is demonstrated that all In₂O₃ sensors exhibit remarkable response to NO₂ gas (In₂O₃-350 shows highest response almost 3200 times), as equated with other intrusive gases. The further discussion regarding high selectivity to NO₂ as shown by In₂O₃ sensor is discussed in sensing mechanism section.

It is equally important to study the impact of humidity on the gas sensing performance, as it may dominant due to the reaction between moisture and oxygen ions present on the surface of sensing materials. Therefore, the time-response humidity study has been performed for In₂O₃-350 in varied humidity environment and under exposure of 2 ppm NO₂ gas at 50 °C. It is examined that as the humidity increased gradually, as 30% RH, 50% RH, 70% RH, and 90% RH, the response of sensor is decreased marginally as shown in Fig. 5c. In detailed, the response of In₂O₃-350 device is decreased from the value of 3224 to 2516, under influence of humidity tuned from 30% RH to 90% RH as depicted in Fig. 5d. The corresponding resistance (R_g) of In₂O₃-350 sensor

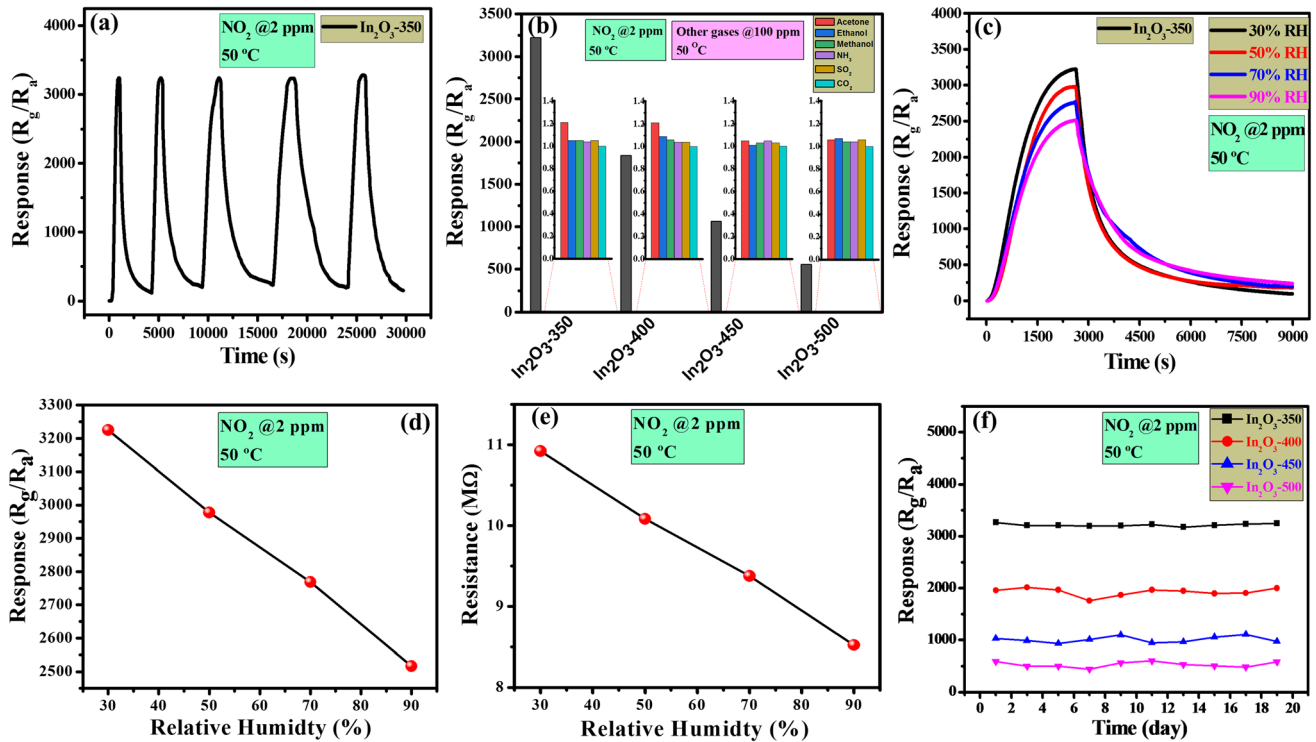


Fig. 5 a Repeatability test for In₂O₃-350 at 2 ppm NO₂ gas; b Selectivity test of In₂O₃-350, In₂O₃-400, In₂O₃-450, and In₂O₃-500 sensors to 2 ppm NO₂ at 50 °C; c Time response curve of In₂O₃-350 sensor under different humidity environment at 2 ppm NO₂ gas; d Response characteristics of In₂O₃-350 sensor in varied

humidity level; e Typical response resistance curve of In₂O₃-350 in different humidity environment, and f Life-time performance test of In₂O₃-350, In₂O₃-400, In₂O₃-450, and In₂O₃-500 sensors to 2 ppm of NO₂ at 50 °C

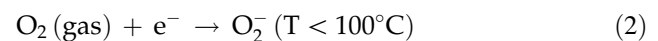
is decreased from 10.9 MΩ to 8.5 MΩ, under humidity change of 30% RH to 90% RH as shown in Fig. 5e. Therefore, the decline in sensor response is not that much significant under such large variation of humidity (varied from 30% RH to 90% RH).

Along with high response of the sensors, the sensors stability is also a crucial parameter in application point of view. Therefore, the long-term stability of In₂O₃-350, In₂O₃-400, In₂O₃-450, and In₂O₃-500 sensors is performed toward 2 ppm NO₂ gas at 50 °C for 19 days as shown in Fig. 5f. During this test, it is detected that all the sensors exhibit highly stable response (response changed from 3267 to 3248 for In₂O₃-350), indicating its potential use for gas sensing applications.

3.4 Gas sensing mechanism

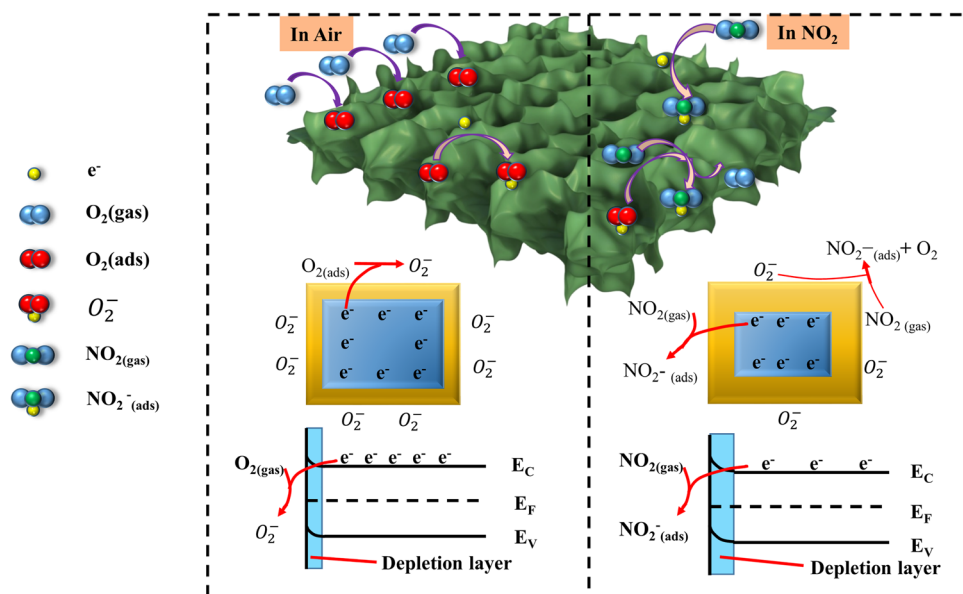
Generally, MOX-based gas detection is relied on alteration in electrical conductivity via surface reactions between oxygen ions present on the sensing layer and oxidized NO₂ gas. The detail mechanism is

discussed in following way. Generally, the electrical conductivity of In₂O₃ is occurred due to an electron transfer between the In²⁺ and In³⁺. The In²⁺ form through the oxygen deficiencies, which are mainly for NO₂ chemisorption. Once the NO₂ chemisorption occurs, the bond is formed between the active sites and orbital of NO₂ and shares the electrons effectively [15, 44]. Thus, the resistance of In₂O₃ increases with respect to increasing adsorption of NO₂. As revealed in Fig. 6, when oxygen gas is physically adsorbed on the surface of In₂O₃, it forms oxygen ions (O₂⁻ (ads)) by accepting electrons from the conduction band of In₂O₃. Thus, oxygen ions on the surface of In₂O₃ become active sites which ensure the effective interaction with NO₂. Depending upon the temperature, the surface redox reactions are as given below [14, 24, 25, 45]:

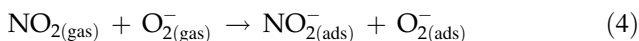
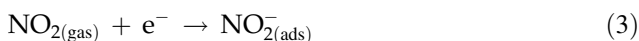


As displayed in Fig. 6, when In₂O₃ device is exposed to NO₂ gas, the oxygen vacancies present on

Fig. 6 The schematic of sensing mechanism of In_2O_3 in air and under the exposure of NO_2 gas



the surface of In_2O_3 vigorously participated in the interaction with NO_2 gas. The surface redox reactions are formed on the sensing surface, in which the NO_2 extracts more and more electrons from the conduction band of In_2O_3 and thus, changes the electrical conductivity through modulation of depletion width. The NO_2 has strong affinity (2.28 eV) comparatively with pre-adsorbed oxygen (0.43 eV) and therefore, can able to capture large number of electrons from In_2O_3 , which additionally increases the thickness of depletion width and hence, the corresponding resistance of the sensing device significantly increases, which is in accordance with our observed experimental results. As more and more NO_2 gas get adsorbed on the surface, the resistance of the sensing device also rises proportionally. The interaction of NO_2 gas with oxygen ions is as shown below [14, 22, 24, 25, 45–47]:



From experimental results, it is confirmed that the In_2O_3 -350 sensor shows highest sensing response as compared with In_2O_3 -400, In_2O_3 -450, and In_2O_3 -500, respectively. There are various reasons to justify its sensing performance. One main factor is the oxygen species present on the sensing surface of In_2O_3 -350. The XPS results revealed that the abundance of O_V and O_C present on In_2O_3 -350 material, which greatly enhanced the sensing performance. It observed that

(From Table SI2) the total percentage of O_V and O_C present on In_2O_3 -350 test sample is much higher than In_2O_3 -400, In_2O_3 -450, and In_2O_3 -500, respectively. The plenty of O_V will offer more free electrons for the reaction between O_C and NO_2 gas and thus, enhance the sensing performance. The role of oxygen vacancies is also confirmed by PL spectra of In_2O_3 -350, In_2O_3 -400, In_2O_3 -450, and In_2O_3 -500, respectively (shown in Figure SI10). The PL pattern of In_2O_3 nanosheets display a strong luminescence peak observed at 580 nm wavelength, signifying that the electrons and holes may recombine on singly and doubly ionized oxygen vacancies [48, 49]. Secondly, the high surface area is also playing a crucial role in deciding the sensing performance. More sites are available to adsorb the NO_2 gas on its surface, and hence, significant change in the electrical conductivity of the sensor is observed with respect to large modulation in the resistance. Thus, overall all the parameters are contributing in enhancing the sensing performance.

4 Conclusions

In summary, a facile and effective solvothermal method has been utilized to synthesis the nanosheets of In_2O_3 -350, In_2O_3 -400, In_2O_3 -450, and In_2O_3 -500. The sensor exhibited excellent gas sensing characteristics, such as very high response, great long-term stability and superior selectivity to NO_2 gas in the

concentration of 5 ppb to 5 ppm at optimized working temperature of 50 °C. The In₂O₃-350 sensor has shown wide sensing bandwidth, very high linearity with obtained response of 1.67/ppb to NO₂ concentration of 5 ppb to 5 ppm, with observed detection limit down to ppb level. The sensor has shown excellent response and selectivity to 2 ppm NO₂ gas, which is about 3200 times higher than the responses shown by other interfering gases. The abundance of oxygen vacancies presents on the surface of In₂O₃ speed-up the reaction kinetics and hence, enhance the sensor response multifold times. This type of NO₂ gas sensor with exceptional sensing characteristics, which could potentially be used in monitoring environment and industrial applications.

Acknowledgements

We acknowledge National Natural Science Foundation of China (Grant Nos. 11774241, 12074263, 51872187, 61704111 and 21805194) and Shenzhen Discipline Layout Project (Grant Nos. JCYJ20170818144212483, JCYJ2018030507182248925 and JCYJ20180508163404043).

Declarations

Conflict of interest There are no conflicts to declare.

Supplementary Information: The online version contains supplementary material available at <http://doi.org/10.1007/s10854-021-06467-4>.

References

- M.T. Vijjapu, S.G. Surya, S. Yuvaraja, X. Zhang, H.N. Alshareef, K.N. Salama, *ACS Sensors* **5**, 984 (2020)
- R. Kumar, R.N. Jenjeti, S. Sampath, *ACS Sensors* **5**, 404 (2020)
- L. Francioso, in edited by K. C. B. T.-N. for C. and B. A. Honeychurch (Woodhead Publishing, 2014), pp. 101–124.
- A. Mirzaei, J.-H. Lee, S.M. Majhi, M. Weber, M. Bechelany, H.W. Kim, S.S. Kim, *J. Appl. Phys.* **126**, 241102 (2019)
- R.K. Jha, N. Bhat, *Adv. Mater. Interfaces* **7**, 2070038 (2020)
- A. Tamvakos, K. Korir, D. Tamvakos, D. Calestani, G. Cicero, D. Pullini, *ACS Sensors* **1**, 406 (2016)
- D.N. Oosthuizen, D.E. Motaung, H.C. Swart, *Sensors Actuators B Chem.* **266**, 761 (2018)
- J. Kaur, R. Kumar, M.C. Bhatnagar, *Sensors Actuators B Chem.* **126**, 478 (2007)
- Y. Gönüllü, G.C.M. Rodríguez, B. Saruhan, M. Ürgen, *Sensors Actuators B Chem.* **169**, 151 (2012)
- B. Urasinska-Wojcik, T.A. Vincent, M.F. Chowdhury, J.W. Gardner, *Sensors Actuators B Chem.* **239**, 1051 (2017)
- D. Peeters, D. Barreca, G. Carraro, E. Comini, A. Gasparotto, C. Maccato, C. Sada, G. Sberveglieri, *J. Phys. Chem. C* **118**, 11813 (2014)
- K. Tian, X.-X. Wang, H.-Y. Li, R. Nadimicherla, X. Guo, *Sensors Actuators B Chem.* **227**, 554 (2016)
- X. Wang, J. Su, H. Chen, G.-D. Li, Z. Shi, H. Zou, X. Zou, *A.C.S. Appl. Mater. Interfaces* **9**, 16335 (2017)
- G. Qu, G. Fan, M. Zhou, X. Rong, T. Li, R. Zhang, J. Sun, D. Chen, *ACS Omega* **4**, 4221 (2019)
- X. Hu, L. Tian, H. Sun, B. Wang, Y. Gao, P. Sun, F. Liu, G. Lu, *Sensors Actuators B Chem.* **221**, 297 (2015)
- J. Liu, S. Li, B. Zhang, Y. Wang, Y. Gao, X. Liang, Y. Wang, G. Lu, *J. Colloid Interface Sci.* **504**, 206 (2017)
- J. Wang, J. Su, H. Chen, X. Zou, G.-D. Li, *J. Mater. Chem. C* **6**, 4156 (2018)
- T. Hyodo, S. Furuno, E. Fujii, K. Matsuo, S. Motokucho, K. Kojio, Y. Shimizu, *Sensors Actuators B Chem.* **187**, 495 (2013)
- B. Xiao, S. Song, P. Wang, Q. Zhao, M. Chuai, M. Zhang, *Sensors Actuators B Chem.* **241**, 489 (2017)
- X. Xu, P. Zhao, D. Wang, P. Sun, L. You, Y. Sun, X. Liang, F. Liu, H. Chen, G. Lu, *Sensors Actuators B Chem.* **176**, 405 (2013)
- L. Gao, Z. Cheng, Q. Xiang, Y. Zhang, J. Xu, *Sensors Actuators B Chem.* **208**, 436 (2015)
- Z. Liu, J. Huang, Q. Wang, J. Zhou, J. Ye, X. Li, Y. Geng, Z. Liang, Y. Du, X. Tian, *Sensors Actuators B Chem.* **308**, 127650 (2020)
- Y. Liu, X. Gao, F. Li, G. Lu, T. Zhang, N. Barsan, *Sensors Actuators B Chem.* **260**, 927 (2018)
- K. Chen, H. Lu, G. Li, J. Zhang, Y. Tian, Y. Gao, Q. Guo, H. Lu, J. Gao, *Sensors Actuators B Chem.* **308**, 127716 (2020)
- Q. Yang, Y. Wang, J. Liu, J. Liu, Y. Gao, P. Sun, J. Zheng, T. Zhang, Y. Wang, G. Lu, *Sensors Actuators B Chem.* **241**, 806 (2017)
- H. Zhang, X. Xu, Y. Zhu, K. Bao, Z. Lu, P. Sun, Y. Sun, G. Lu, *RSC Adv.* **7**, 49273 (2017)
- M. Cheng, Z. Wu, G. Liu, L. Zhao, Y. Gao, B. Zhang, F. Liu, X. Yan, X. Liang, P. Sun, G. Lu, *Sensors Actuators B Chem.* **291**, 216 (2019)
- X. Liu, K. Zhao, X. Sun, C. Zhang, X. Duan, P. Hou, G. Zhao, S. Zhang, H. Yang, R. Cao, X. Xu, *Sensors Actuators B Chem.* **285**, 1 (2019)

29. X. Liu, L. Jiang, X. Jiang, X. Tian, Y. Huang, P. Hou, S. Zhang, X. Xu, *Appl. Surf. Sci.* **447**, 49 (2018)
30. P. Li, C. Cai, T. Cheng, Y. Huang, *RSC Adv.* **7**, 50760 (2017)
31. X. Liu, X. Tian, X. Jiang, L. Jiang, P. Hou, S. Zhang, X. Sun, H. Yang, R. Cao, X. Xu, *Sensors Actuators B Chem.* **270**, 304 (2018)
32. Z. Wang, C. Hou, Q. De, F. Gu, D. Han, *ACS Sensors* **3**, 468 (2018)
33. F. Gu, C. Li, D. Han, Z. Wang, *A.C.S. Appl. Mater. Interfaces* **10**, 933 (2018)
34. K. Wan, D. Wang, F. Wang, H. Li, J. Xu, X. Wang, J. Yang, *A.C.S. Appl. Mater. Interfaces* **11**, 45214 (2019)
35. D. Han, L. Zhai, F. Gu, Z. Wang, *Sensors Actuators B Chem.* **262**, 655 (2018)
36. Y. Xia, J. Wang, J.-L. Xu, X. Li, D. Xie, L. Xiang, S. Komarneni, *A.C.S. Appl. Mater. Interfaces* **8**, 35454 (2016)
37. J. Pan, W. Liu, L. Quan, N. Han, S. Bai, R. Luo, Y. Feng, D. Li, A. Chen, *Ind. Eng. Chem. Res.* **57**, 10086 (2018)
38. M. Wang, Y. Wang, X. Li, C. Ge, S. Hussain, G. Liu, G. Qiao, *Sensors Actuators B Chem.* **316**, 128050 (2020)
39. W. Zeng, Y. Liu, J. Mei, C. Tang, K. Luo, S. Li, H. Zhan, Z. He, *Sensors Actuators B Chem.* **301**, 127010 (2019)
40. D.V. Ponnuruvelu, B. Pullithadathil, A.K. Prasad, S. Dhara, K. Mohamed, A.K. Tyagi, B. Raj, *J. Mater. Sci. Mater. Electron.* **28**, 9738 (2017)
41. B. Xiao, D. Wang, F. Wang, Q. Zhao, C. Zhai, M. Zhang, *Ceram. Int.* **43**, 8183 (2017)
42. C.W. Zou, J. Wang, W. Xie, *J. Colloid Interface Sci.* **478**, 22 (2016)
43. X. Xu, H. Zhang, X. Hu, P. Sun, Y. Zhu, C. He, S. Hou, Y. Sun, G. Lu, *Sensors Actuators B Chem.* **227**, 547 (2016)
44. J. Ri, X. Li, C. Shao, Y. Liu, C. Han, X. Li, Y. Liu, *Sensors Actuators B Chem.* **317**, 128194 (2020)
45. W. Li, J. Guo, L. Cai, W. Qi, Y. Sun, J.-L. Xu, M. Sun, H. Zhu, L. Xiang, D. Xie, T. Ren, *Sensors Actuators B Chem.* **290**, 443 (2019)
46. C.W. Na, J.-H. Kim, H.-J. Kim, H.-S. Woo, A. Gupta, H.-K. Kim, J.-H. Lee, *Sensors Actuators B Chem.* **255**, 1671 (2018)
47. H. Wang, L. Zhou, Y. Liu, F. Liu, X. Liang, F. Liu, Y. Gao, X. Yan, G. Lu, *Sensors Actuators B Chem.* **305**, 127498 (2020)
48. S.-T. Jean, Y.-C. Her, *Cryst. Growth Des.* **10**, 2104 (2010)
49. P. Papageorgiou, M. Zervos, A. Othonos, *Nanoscale Res. Lett.* **6**, 311 (2011)

Publisher's Note Springer Nature remains neutral with regard to jurisdictional claims in published maps and institutional affiliations.